PAPER

On defects' role in enhanced perpendicular magnetic anisotropy in Pt/Co/Pt, induced by ion irradiation

IOP Publishing Journal of Physics: Condensed Matter
J. Phys.: Condens. Matter **31** (2019) 185801 (13pp) https://doi.org/10.1088/1361-648X/ab0351

On defects' role in enhanced perpendicular magnetic anisotropy in Pt/Co/Pt, induced by ion irradiation

M M Jakubowski[1], M O Liedke[2], M Butterling[2], E Dynowska[1], I Sveklo[3], E Milińska[1], Z Kurant[3], R Böttger[4], J von Borany[4], A Maziewski[3], A Wagner[2] and A Wawro[1]

[1] Institute of Physics, Polish Academy of Sciences, Warsaw, Poland
[2] Institute of Radiation Physics Helmholtz-Zentrum Dresden-Rossendorf, Dresden, Germany
[3] Faculty of Physics, University in Białystok, Białystok, Poland
[4] Institute of Ion Beam Physics and Materials Research, Helmholtz-Zentrum Dresden-Rossendorf, Dresden, Germany

E-mail: marcin.jakubowski@ifpan.edu.pl

Received 6 November 2018, revised 16 January 2019
Accepted for publication 30 January 2019
Published 5 March 2019

Abstract

Modifications of magnetic and magneto-optical properties of Pt/Co($\mathbf{d_{Co}}$)/Pt upon Ar^+ irradiation (with energy 1.2, 5 and 30 keV) and fluence, **F** at the range from $2 \cdot 10^{13}$–$2 \cdot 10^{16}$ Ar^+ cm^{-2}) were studied. Two 'branches' of increased perpendicular magnetic anisotropy (PMA) and enhanced magneto-optical response are found on 2D ($\mathbf{d_{Co}}$, **F**) diagrams. The difference in **F** between 'branches' is driven by ion energy. Structural features correlated with magnetic properties have been analysed thoroughly by x-ray diffraction, Rutherford backscattering spectrometry and positron annihilation spectroscopy. Experimental results are in agreement with TRIDYN numerical calculations of irradiation-induced layers intermixing. Our work discusses particularly structural factors related to crystal lattice defects and strain, created and modified by irradiation, co-responsible for the increase in the PMA.

Keywords: vacancy formation, Rutherford backscattering, RBS, positron spectroscopy, Ion irradiation, magnetic thin films, lattice strains, perpendicular magnetic anisotropy, PMA

Supplementary material for this article is available online

(Some figures may appear in colour only in the online journal)

Introduction

Thin magnetic films with their functionality can be enhanced by ion irradiation, what can lead to a modification of perpendicular magnetic anisotropy (PMA) [1–3]. This is very promising for the engineering of preferred properties in a local scale for emerging applications, i.e. for out-of-plane nanomagnet logic (oNML) devices [4], shift registers [5], magnetic patterning [6] or device prototyping [7] and more. Moreover, the studies of ultrathin films with PMA on the explanation of the fundamental physics, i.e. the Dzyaloshinskii–Moriya (DMI) interactions [8, 9], is still present in very recent reports.

Symmetrical covers of Pt, induce in Pt/Co/Pt strong PMA, orienting out-of-plane magnetization up to Co layer critical thickness $\mathbf{d_{SRT}}$. While decreasing cobalt thickness, $\mathbf{d_{Co}}$ below $\mathbf{d_{SRT}}$ (ca. 1.9 nm), a spin reorientation transition (SRT) [10] from in-plane to out-of-plane magnetization alignment takes place. Initial works on ion irradiation of Pt/Co/Pt reported a decrease in PMA [11, 12] upon treatment. Previous works on homogeneously irradiated Pt/Co/Pt or $[Pt/Co]_N$ multilayers employed low (10–30 keV) or high energy (0.15–2 MeV) ions of several ion spices including i.e. He^+ [11–15], Ar^+ [13, 16, 17], Ga^+ [2, 3, 13, 18], N^+ [19], Xe^+ [20], Kr^+ [21], O^+ and Ag^+ [22] or Cr^+ [21]. As was shown, with $\mathbf{d_{Co}} < \mathbf{d_{SRT}}$, ion

irradiation leads to diminishing PMA [11, 14, 18], and further to transition into a paramagnetic state. These effects were utilized as a demonstration for fabricated out-of-plane patterned media [23–26]. However, an opposite modification, i.e. reorientation of magnetization from in-plane to perpendicular alignment was also reported for Ga^+ [2]. Under 30 keV Ga^+ ion irradiation, a sequential increase of the PMA with the ion fluence, **F** increases, (visible as 'branches' of the higher value of remanence magnetisation, on the 2D magnetisation remanence map, $m_R(\mathbf{F}, \mathbf{d_{Co}})$) has been observed [3, 27]. This was explained by competition between the interface degradation [3, 28], the magnetoelastic effect induced by lattice strain [28, 29], alloy formation with strong PMA [3, 28, 30, 31] and Co nanodiscs [32]. However, full structural aspects of lattice distortion and their impact on the PMA changes upon ion irradiation modifications in ultrathin film structures are extremely difficult to analyse, where a small volume of the sample makes standard techniques non-sensitive or inaccurate.

The goal of this work is to explore the possibility to induce PMA in ultrathin Co by Ar^+ ions bombardment instead of Ga^+ ions [3]. Ar^+ ions irradiation sources are commonly available in technological systems. We selected Ar^+ ions of energy 1.2, 5 and 30 keV enabling studies of precise nanostructure modifications on different depth in relation to magnetic layer position. We establish a correlation between the magnetic and structural changes of Pt/Co/Pt ultra-thin layered structure induced by irradiation with Ar^+ ions. Applied locally probing magneto-optical Kerr effect (MOKE) technique in polar configuration (PMOKE), which enables investigations of magnetic properties as a function of $\mathbf{d_{Co}}$ and **F**. Evolution of the structural modifications under irradiation has been analysed using x-ray diffraction (XRD), Rutherford backscattering spectrometry (RBS) and also illustrated by numerical simulations with use of binary collision approximation (BCA) code TRIDYN [33]. The unique properties of positron interaction with the thin film surface region have been utilized, in positron annihilation spectroscopy (PAS) [34–37] for the defect spectroscopy of the ion irradiated samples. Lattice defects such as vacancies can be determined, i.e. optical and electronic properties of materials to a large extent. Our work opens the interpretation where defects creation, alloy formation and strain generation can be correlated to observed magneto-optical properties and the PMA.

1. Experimental

1.1. Samples growth and in situ characterisation

The Pt(30 nm)/Co($\mathbf{d_{Co}}$)/Pt(5 nm) samples were grown by molecular beam epitaxy (MBE). Samples with Co layer, $\mathbf{d_{Co}} = 0$–5 nm were investigated by local probing methods (figure 1(a)). Additional samples with a uniform thickness of $\mathbf{d_{Co}} = 3$ nm were grown for nonlocal probing techniques (figure 1(b)). Crystal structure of the samples was investigated *in situ* (figure 2) by means of reflection high-energy electron diffraction (RHEED), low-energy electron diffraction (LEED) and scanning tunnelling microscopy (STM).

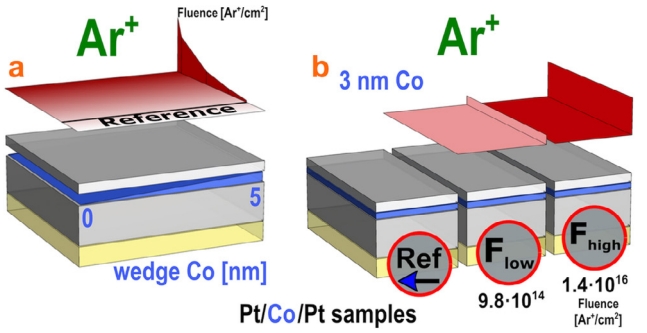

Figure 1. Two types of samples with varied (a) and homogenous (b) Ar^+ irradiation. Brief irradiation scheme and samples description.

1.2. Ion irradiation

Ion modification of the samples has been performed using ion implanter with gaseous Ar source extractor. To achieve ion fluence, **F** gradient irradiation, ranging from $2 \cdot 10^{13}$ to $1.9 \cdot 10^{16}$ Ar^+ cm^{-2}, a linear shutter has been placed directly in above of the sample. Ion energies 1.2, 5 and 30 keV were used. Orthogonal orientation of $\mathbf{d_{Co}}$ and **F** gradients allow constructing false colour maps of magnetic properties, depending on $\mathbf{d_{Co}}$ and **F** (figure 1(a)). Additionally, in order to examine structural changes upon ion irradiation and associated with them observed magnetooptical properties, the uniform samples $Pt/Co_{(3nm)}/Pt$ were irradiated uniformly (figure 1(b)) with ion fluences: $9.8 \cdot 10^{14}$ ($\mathbf{F_{low}}$) and $1.45 \cdot 10^{16}$ ($\mathbf{F_{high}}$) ions cm^{-2} and energy 30 keV. A non-irradiated (**Ref**), as-grown sample, served as a reference.

1.3. Samples characterisation methods

Samples were studied using MOKE setup, in polar configuration (see supplementary materials (SM) S1 (stacks.iop.org/JPhysCM/31/185801/mmedia)). Structural properties of the additional samples (figure 1(b)), before and after ion irradiation, were examined *ex situ* by 1.2 MeV He^+ RBS [38–40] with channelling (c-RBS) methods. Elements concentration, [at%] depth profiles were calculated using SIMNRA [41, 42] software simulations and supported by SimTarget applet [43]. The symmetrical and asymmetrical XRD measurements allow determining the strain states and relaxed lattice parameters of the Pt and $Pt_{1-x}Co_x$ layers before and after ion irradiation, respectively. Finally, PAS analysis of ion irradiation induced defects has been performed at the slow-positron system of Rossendorf (SPONSOR) [44, 45], which provides a tungsten foil moderated (monoenergetic), magnetically guided variable energy positron beam. We have utilized Doppler-broadening spectroscopy of the positron-electron annihilation line (PAS-DBS) and coincident (PAS-cDBS) at fixed energy (1.88 keV), that allow us to get more information about sample defect creation by ions [34–37] In order to quantify defects size thicker MBE-grown Co and Pt reference films, deposited at the same condition as ion irradiated samples, have been measured by means of positron annihilation lifetime spectroscopy (PALS) at the mono-energetic positron spectroscopy

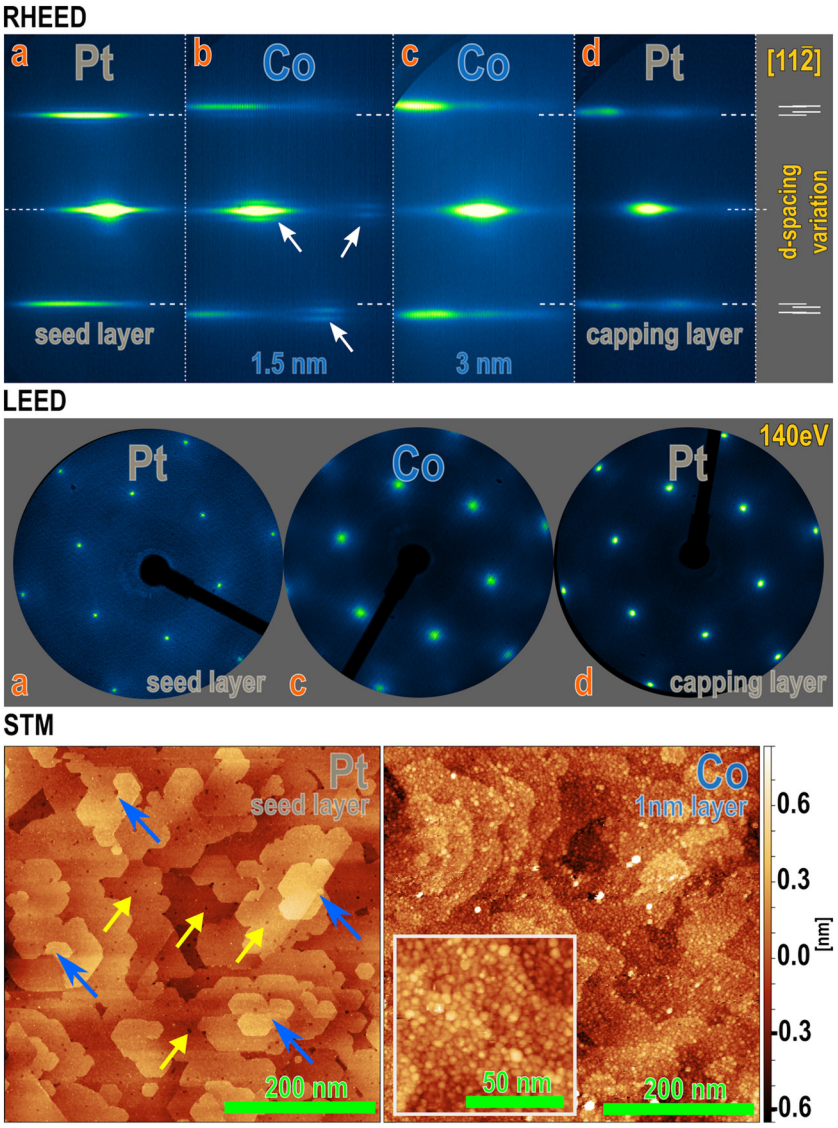

Figure 2. The MBE growth of Pt/Co/Pt films. Epitaxy characterisation using RHEED and LEED of Pt seed layer (a), 1.5 and 3 nm Co layer ((b) and (c) respectively) and Pt capping layer (d). Constant current STM surface images of Pt seed layer and 1 nm of Co layer (bottom). Arrows—see text.

(MePS) beamline, at the radiation source ELBE (Electron Linac for beams with high Brilliance and low Emittance) at HZDR, Germany [46].

2. Results

2.1. In situ sample characterisation

In situ diffraction patterns (figure 2), RHEED streaks and LEED sharp spots of virgin Pt/Co/Pt, indicate the very good structural quality of the virgin samples. *In situ* STM topography images (figure 2) of Pt seed surface shows atomic steps with edges align with crystallographic directions with few screw dislocations (blue arrows) and vacancy islands [47] (yellow arrows). The slightly broadened and partly split RHEED streaks (white arrows), originated from the Co layer, indicate small islands formation that has preferred separation [48], at the initial growth stage. This dense nucleation due to growth at room temperature, that disappears after ~2 nm of the film coverage, was visible as diffusive streaks in RHEED pattern, originate from the less coherent surface with small epitaxial grains. Finally, RHEED pattern of Pt cap layer that has presumably wavy and grainy surface shown even more blurred streaks. Moreover, strain evolution during MBE growth process was observed as a d-spacing variation deduced from RHEED streak spacing distances (see SM S2).

2.2. Magneto-optical characterisation

Figure 3 shows a set of ($\mathbf{d_{Co}}$, **F**) maps of magnetic parameters for samples irradiated by Ar^+ ions with three chosen energies. Magneto-optical parameters illustrated in figure 3 are defined in SM S1, similarly to reported elsewhere [3]. At the bottom of each map, an area corresponding to magneto-optical parameters of the non-irradiated sample has been shown as a reference for the comparison. The SRT thickness

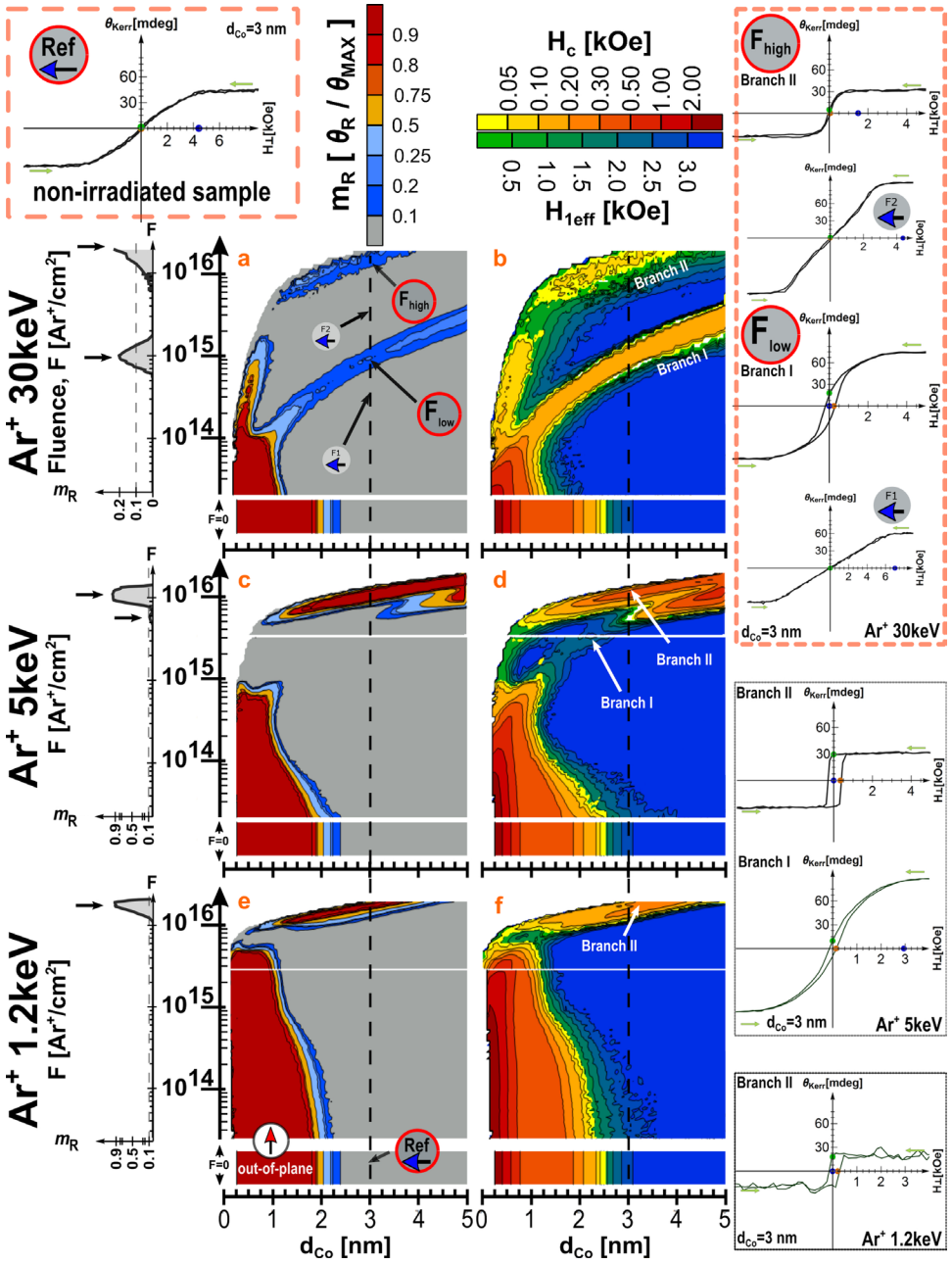

Figure 3. Magnetic properties of Pt/Co_{wedge}/Pt samples, Ar^+ irradiated with 1.2 (a)–(c), 5 (d)–(f) and 30 keV (g)–(i) ion energies, presented as a set of ($\mathbf{d_{Co}}$, **F**) diagrams of max remanence magnetisation m_R (a), (c) and (e), effective anisotropy H_{1eff} (green-blue scale) fields together with coercive field H_C (yellow–red scale) (b), (d) and (f). H_{1eff} is defined only for $H_{1eff} < 0$ values. The left panel shows m_R ($Co_{3\ nm}$, F) trend lines for all ion energies, with an indication of characteristic points 'Branch I' and 'Branch II'—corresponding θ_{Kerr}-H loops are presented (right side). M–H loop easy plane (in-plane) for non-irradiated **Ref** sample. The **Ref**, $\mathbf{F_{low}}$ and $\mathbf{F_{high}}$ marks correspond to the magnetic parameters of homogeneously irradiated samples with the same names.

coincides with a position of the transition area between dark red and grey colours at normalized remanence, m_R map (i.e. figure 3(a), $\mathbf{d_{Co}} = \mathbf{d_{SRT}} \approx 1.9$ nm). Presented maps for Ar^+ 30 keV modifications reveal two clearly separated 'branches' of the enhanced PMA, expressed i.e. in the presence of a perpendicular m_R component to magnetisation vector, similarly to reported 30 keV Ga^+ irradiation [3] effects. However, corresponding features appear at higher Ar^+ fluences. In the central part of the maps, a lower fluence 'Branch I' extends towards increasing **F** and thicker $\mathbf{d_{Co}}$. A higher fluence 'Branch II' occurs in the upper part of the maps adjacent to a border between magnetic and non-magnetic part of the sample (out of colour scale). **F** as low as 10^{13} ion cm^{-2} substantially reduces the $\mathbf{d_{SRT}}$ (ca. $\mathbf{d_{Co}} \approx 1.1$ nm), where the SRT occurs. With the ion energy decreasing (1.2 and 5 keV), the 'Branch I' is shifted towards higher fluences. The lowest fluences (i.e. 10^{13} ions cm^{-2}) with energies of 1.2 and 5 keV do not affect the $\mathbf{d_{SRT}}$ markedly, contrary to 30 keV. Presumably, due to limited ion range of modification, lower energy ions gradually shifts the $\mathbf{d_{SRT}}$, with **F** increasing, towards ca. $\mathbf{d_{Co}} \approx 1.1$ nm. Finally, at the lowest ion energy (1.2 keV) only a single 'branch' is observed. For all three ion energies used in the experiment,

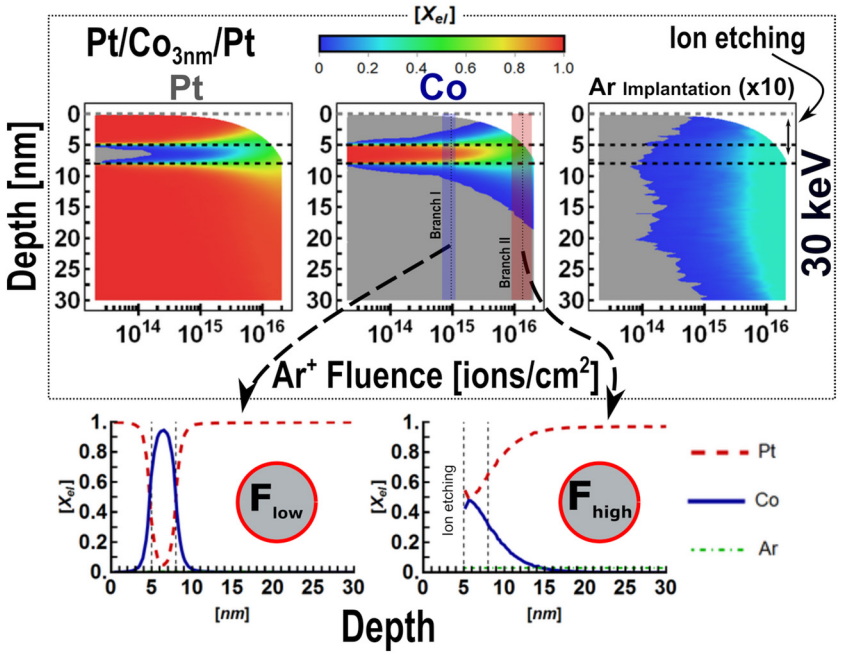

Figure 4. TRIDYN in-depth element concentration profiles corrected by surface ion etching. Colour scales are the same for all of the elements; dashed black lines indicate virgin Pt/Co interfaces. Vertical beams correspond to 'Branch I' (blueish) and 'Branch II' (reddish) respectively with indicated by the arrows discrete in-depth element concentration profiles for selected ion fluences—$\mathbf{F_{low}}$ and $\mathbf{F_{high}}$.

the m_R ($\mathbf{d_{Co}} = 3$ nm, **F**) profiles are shown on the left side of the illustration with arrows indicating 'branches' of enhanced PMA. On the right side, PMOKE *M–H* ($\mathbf{d_{Co}} = 3$ nm, **F**) corresponding to the observed 'branches'. Moreover, top-left corner shows *M–H* ($\mathbf{d_{Co}} = 3$ nm, non-irradiated) hysteresis for the non-treated sample (**Ref**). In particular, the in-plane magnetized sample ($\mathbf{d_{Co}} = 3$ nm) where **F** increase induces two 'branches' of enhanced PMA, points of interest were arbitrary selected, with maximal values of H_C and m_R with fluences $\mathbf{F_{low}}$, $\mathbf{F_{high}}$ (see experimental and figure 1(b)). More analysis, specifically the 'Branch I' of 30 keV sample and $\theta_{max}(\mathbf{d_{Co}}, \mathbf{F})$ map, can be found in SM S1.

2.3. TRIDYN simulations

The main part of our analyses we focused on the 3 nm Co samples, 30 keV Ar^+ and $\mathbf{F_{low}}$ and $\mathbf{F_{high}}$ irradiated, where the separation of two 'branches' is observed (figure 3(a)), to searching for the causes of magnetic changes in the structural modification of layers. So first, we run the TRIDYN simulations (figure 4) in order to estimate changes in concentration, X_{el} (el = Pt, Co and Ar) upon increasing **F** of Ar^+, used in the experiment. A clear intermixing at both interfaces even for the lowest applied **F** of 10^{13} ions cm^{-2} is found at 30 keV Ar^+. The Co layer degradation starts at **F** as low as $2 \cdot 10^{14}$ ions cm^{-2}, where Pt atoms are driven into the layer by intermixing process ($X_{Pt} > 0.01$). The upper bent edges of the maps reflect surface etching. The areas correlated with observed 'branches' of PMA (see figure 3) are shown as shaded vertical stripes. The simulation results of 1.2 and 5 keV Ar^+ and details of the TRIDYN numerical simulations can be found in SM S3.

2.4. XRD characterisation

Structural changes were also checked experimentally by XRD (figure 5). As-grown **Ref** sample and samples irradiated with $\mathbf{F_{low}}$ and $\mathbf{F_{high}}$ were examined (figure 1(b)). The relaxed lattice parameters of all layers before and after irradiation were determined on the base of symmetrical 2 2 2 and asymmetrical 1 1 3 reflections, which enabled calculation of the composition of $Pt_{1-x}Co_x$ alloys and strain (table 1). Obtained results confirmed the [1 1 1] growth direction of the Pt layers. On the base of negative in-plane lattice strain, ε_{xx} of Pt in **Ref** sample, it was concluded that the Pt layer is under compressive strain. The Ar^+ irradiation diminishes the Laue oscillations in both cases $\mathbf{F_{low}}$ and $\mathbf{F_{high}}$ but this effect is a little stronger for $\mathbf{F_{low}}$. This means that irradiation deteriorates the thickness of coherent Pt atomic layers. Moreover, partial interface mixing based on methods described elsewhere [49, 50] can be used for alloy composition calculations (see SM S4). On the base of Pt 222 peak deconvolution, we conclude that two layers can be distinguished. Capping layer thin alloy-layer L_{SA} and relatively thick Pt layer (L_{Pt}) in $\mathbf{F_{low}}$ sample. Similarly, in $\mathbf{F_{high}}$, L_{H1} and L_{H2} can be distinguished.

2.5. RBS characterisation

Further analysis of the composition and structure were done using RBS experiment result, shown in figure 6 for non-irradiated **Ref** (a), irradiated with $\mathbf{F_{low}}$ (b) and $\mathbf{F_{high}}$ (c) samples. This technique is an element and an in-depth position sensitive and highly accurate [38]. Data corresponding to the sapphire substrate is reduced in presented figures for clarity. RBS, c-RBS and SIMNRA simulated RBS spectra were

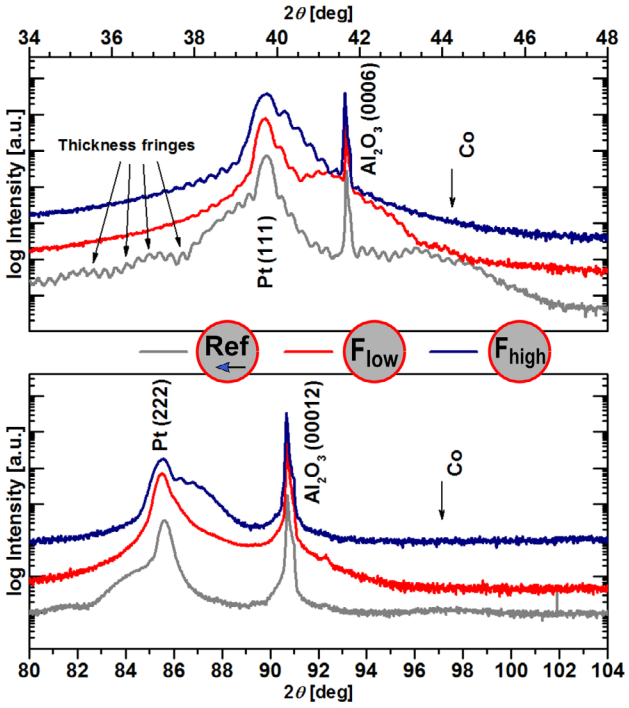

Figure 5. An XRD symmetrical XRD data of as-deposited (**Ref.**) (grey), $\mathbf{F_{low}}$ and $\mathbf{F_{high}}$ samples.

plotted together. For **Ref** sample, the simulated spectrum of Pt layers (seed and capping) is shown separately (dotted line in figure 6(a), see SM S5). In-depth composition profiles (at. %), corresponding to the best fit SIMNRA spectra simulations are shown as figure insets. The characteristic energies, as at the sample surface, for Pt, Co and Ar are marked by the arrows (atoms deeper in the sample result in a signal with lower energy). Since this technique is more sensitive to large Z elements, Pt peak is the strongest. The signal from Co is much weaker as the Co has lower Z and layer is only a small volume of the whole sample. The RBS Pt peak for **Ref** sample is slightly asymmetrical due to the overlapping of both Pt layers signals and Co layer between them. The right-hand slope of the c-RBS Pt peak, related to the vicinity of the sample surface, becomes stronger in the sample irradiated with $\mathbf{F_{low}}$ indicating a disturbed crystal lattice at the surface region of the sample. When $\mathbf{F_{high}}$ is applied, the RBS Pt peak became more symmetrical and c-RBS weak again. However, the c-RBS Pt signal from all samples is much weaker than RBS for all samples, indicating good crystal structure, with two c-RBS peaks visible, related to surface and de-channelling struggling. Generally, the c-RBS signal becomes slightly stronger for $\mathbf{F_{low}}$ and $\mathbf{F_{high}}$ than for **Ref** sample. However, $\mathbf{F_{low}}$ causes an increase in a greater extent, especially higher energy peak ('surface peak'). In addition, in $\mathbf{F_{low}}$ sample shows only slight intermixing, visible at the interfaces (inset figure 6(b)). Evident layer mixing is found in $\mathbf{F_{high}}$ (inset figure 6(c)). For $\mathbf{F_{low}}$ and $\mathbf{F_{high}}$ samples, Ar trace implantation was observed (see SM S5), however only for $\mathbf{F_{high}}$ was possible to determine (using SimTarget) retained dose at $6.3 \cdot 10^{15}$ at cm^{-2}.

2.6. PAS characterisation

Crystal imperfection defects were analysed by the PAS-DBS and PAS-cDBS methods. Interpretation of depth sensitivity for PAS investigated Pt/Co/Pt samples (**Ref**, $\mathbf{F_{low}}$, $\mathbf{F_{high}}$) can be explained on the basis of the so-called Makhovian implantation profile (figure 7(a) and SM S6). DBS S(E) plot (figure 7(b)) gathers results of as-grown **Ref** and irradiated, $\mathbf{F_{low}}$ and $\mathbf{F_{high}}$ samples. Data were fitted using the VEPFIT [51] code. The detailed formalism is explained in SM S6 and elsewhere [52, 53]. The DBS plot shape for the as-grown film (**Ref**) resembles two layers and substrate system, so Co is not easily distinguishable. Although, figure 7(a) shows the energy regime for the Co layer. Definitely, the top Pt layer ($E < 1$ keV) and Al_2O_3 substrate ($E > 3.4$ keV) are well visible as decreasing slopes. After $\mathbf{F_{low}}$ ion fluence, S increases in the lower energy range ($0.5 < E < 2.5$ keV) and the local maximum at $E = 3.4$ keV vanishes, which suggests a slight defect concentration increase in the top Pt/Co part of the sample and decomposition of edge dislocations at the interface into different entities, respectively. The sensitivity of positrons to defects was shown for example in single crystal Cr_2O_3/Al_2O_3 systems [53] which could be analogues here. $\mathbf{F_{high}}$ ion fluence, on the other hand, causes complete intermixing, since the layer structure is mostly invisible, instead, the S-parameter decreases semi-monotonically with different slopes across the metallic film and the substrate. In figure 7(c) several characteristic positron implantation energies corresponding to a trilayer thickness region for each sample are plotted as S–W representation. The S–W plot allows visualizing relative changes in open volume defect types. As long as the data points lay on a single line along with reference samples ($Pt_{(bulk)}$, $Pt_{(MBE)}$, $Co_{(bulk)}$ and $Co_{(MBE)}$—exhibit low defect concentrations and known defect configuration what was presented in SM S6), a single defect type is expected. In figure 8(a) the cDBS ratio plots normalized to the Pt reference ($Pt_{(bulk)}$) spectrum electron momentum distributions (longitudinal component, p_L) are presented for the as-grown (**Ref**) and ion irradiated films ($\mathbf{F_{low}}$, $\mathbf{F_{high}}$) as well as low-defect reference cases of MBE grown and annealed Pt, Co thick layers and Co bulk sample ($Pt_{(MBE)}$, $Co_{(MBE)}$, $Co_{(bulk)}$, respectively). The cDBS spectra have been taken at $E = 1.88$ keV (see figures 7(a) and (b)) where large sensitivity to the thin Co layer is expected. From the low momentum range ($p_L < 5 \cdot 10^{-3}$ m_0c) defect concentration can be assessed and it is clearly increasing with the ion fluence (figure 8(a) inset). The high momentum range for $p_L > 10 \cdot 10^{-3}$ m_0c refers to the electronic fingerprint of elements surrounding the defect site. It is clear that initial larger Pt occupation of the defect site decreases as a function of ion fluence and becomes a combination of both Co (see a minimum at about $p_L \sim 11 \times 10^{-3}$ m_0c) and Pt electronic structure ($p_L \sim 15$–20×10^{-3} m_0c). We have confirmed this to a large extent by theoretical calculations of the positron lifetimes, which were performed within the so-called standard scheme employing the atomic superimposition (ATSUP) method [54, 55]. Atomic relaxations in the vicinity

Table 1. Results of the XRD measurements: relaxed lattice parameters, the composition of alloys and strain states of the layers.

Sample		Lattice spacing d_{222} (Å)	Lattice spacing d_{113} (Å)	Relaxed lattice parameter a_{rel} (Å)	Composition $Pt_{1-x}Co_x$ x	Strain ε_{xx}	Strain ε_{zz}
						err $\pm 5 \times 10^{-2}$%	
Ref as grown		1.1335(2)	1.1823(2)	3.913(4)	0	−0.18%	0.35%
$\mathbf{F_{low}}$ $9.8 \cdot 10^{14}$ Ar^+ cm^{-2}	L_{SA} (top)	1.1290(2)	1.1780(2)	3.900(4)	0.10(2)	▲ −0.14%	▼ 0.28%
	L_{Pt} (bottom)	1.1346(2)	1.1830(2)	3.913(4)	0	▼ −0.20%	▼ 0.44%
$\mathbf{F_{high}}$ $1.45 \cdot 10^{16}$ Ar^+ cm^{-2}	L_{H1} (top)	1.1200(2)	1.1710(2)	3.891(4)	0.13(2)	▼ 0.14%	▼ −0.28%
	L_{H2} (bottom)	1.1340(2)	1.1818(2)	3.905(4)	0.07(2)	▼ −0.31%	▼ 0.60%

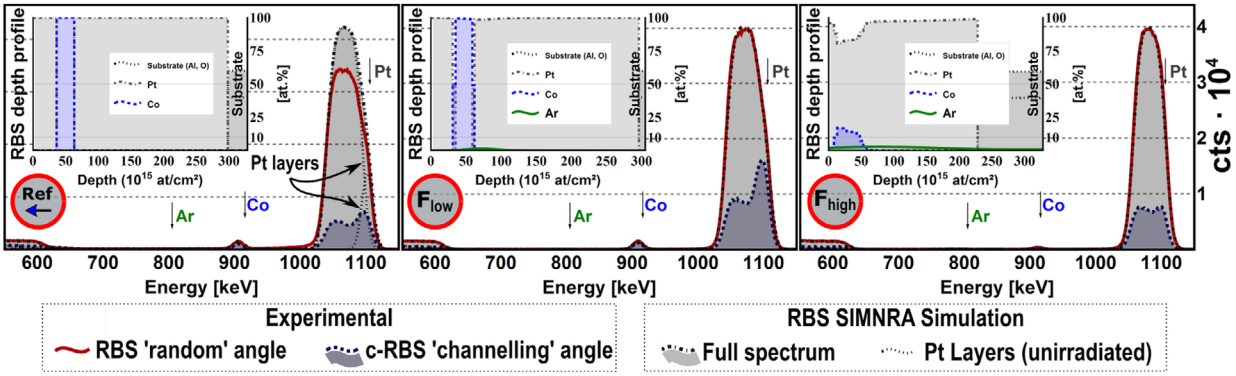

Figure 6. RBS and c-RBS spectra of irradiated $Pt/Co_{3\ nm}/Pt$ samples. Depth profiles of elements concentration [at %] corresponding to random RBS experimental data are illustrated as insets. Arrows marked by element symbols point the energies of scattered 1,2 MeV He^+ ions from the first atomic layer.

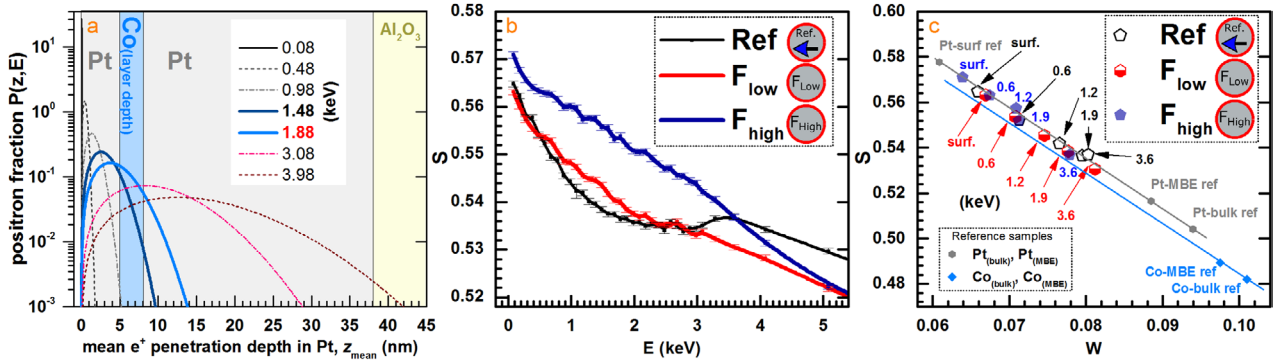

Figure 7. PAS-DBS results for **Ref.**, $\mathbf{F_{low}}$ and $\mathbf{F_{high}}$ samples.

of a defect have been not considered in our calculations. Several different cases have been simulated (see figure 8(b)): defect-free Co (A3); Pt (A1); Pt_3Co ($L1_2$); PtCo $L1_0$ with four Co atoms per unit cell; PtCo $L1_0$ Pt-rich, with only one Co per unit cell; and cases with vacancies Co-monovacancy (Co A3 v_{Co}); Pt-monovacancy (Pt A1 v_{Pt}); and finally PtCo $L1_0$ Pt-rich, with a three-vacancy complex of neighboring Co–Pt–Pt atoms (PtCo $L1_0$ Pt-rich $v_{Co–Pt–Pt}$). The right part and the inset of figure 8(b) depicts unit cells of close-packed Pt and Co alloy structures with defect-free (right) and consisting mentioned three-vacancy complex (inset) structures that were utilized for the ATSUP simulation. Atom elements and defects type are defined in the legend of illustration. In general, the most standard scheme of ATSUP cannot precisely describe positron annihilation with low momentum valence electrons, $p_L < 10 \cdot 10^{-3}$ m_0c, however, it can fully predict trends once vacancy states are introduced into a system. The high electron momentum region, $p_L > 10 \cdot 10^{-3}$ m_0c, which is of the main interest here, can be reliably calculated and with good agreement between experimental data (figure 8(a)) and simulations (figure 8(b)) is found. Especially, the monovacancy states in both Co and Pt MBE grown samples nicely overlap with the experimental data even in the low electron momentum range. This clearly demonstrates the existence of vacancies and possibly dislocations in the MBE grown reference samples, which usually have very similar positron lifetime, thus are difficult to separate.

3. Discussion

Previously suggested, different origins for the appearance of the enhanced PMA in the two 'branches' [27] are also confirmed by our results concerning Ar^+ irradiation. In our

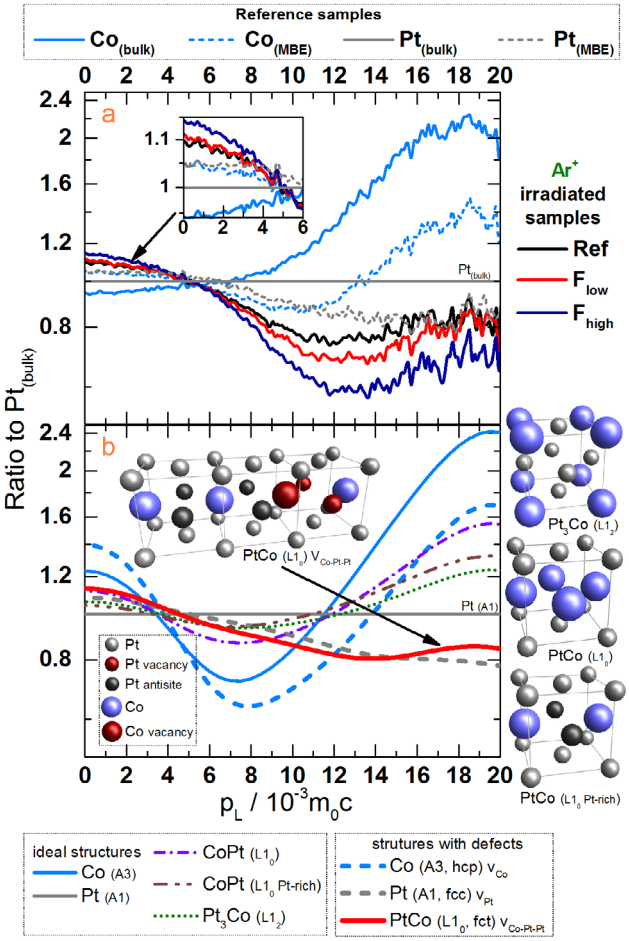

Figure 8. PAS-cDBS ratio plots normalized to the defects free $Pt_{(bulk)}$ reference sample (a) and unit cells of close-packed structures utilized for the ATSUP simulation of the cDBS ratio plots (b).

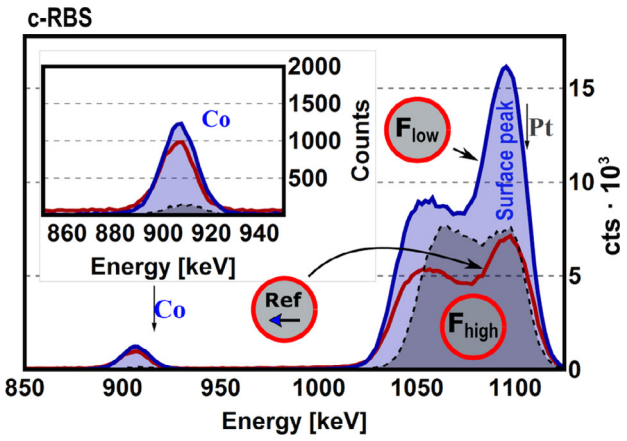

Figure 9. c-RBS spectra comparative analysis of all measured $Pt/Co_{3\ nm}/Pt$ samples.

experiment, we have focused on $\mathbf{F_{low}}$ and $\mathbf{F_{high}}$ samples that correspond to both of the 'branches'. Observed structural differences encompass various defect concentrations, lattice stress states and alloying of the Co ferromagnetic layer. In the case of $\mathbf{F_{low}}$, enhanced PMA is mainly due to ion-induced in-plane tensile strain and limited interface mixing. Under $\mathbf{F_{high}}$ irradiation, PMA is triggered by intense mixing, ferromagnetic layer thickness change and noticeable changes in the sample surface. A detailed discussion of structural modifications induced by $\mathbf{F_{low}}$ and $\mathbf{F_{high}}$ of 30 keV ions and possible processes occurring due to irradiation is presented below.

3.1. F_{low}—'Branch I'

In $\mathbf{F_{low}}$, alloy formation is low, in the vicinity of Co interfaces, as it was shown experimentally by RBS and XRD, and qualitatively confirmed by the change in concentration at the interfaces by TRIDYN, simulations. More precisely, a close look upon the RBS Pt and Co signal clearly suggest only partial ion mixing of Co layer in $\mathbf{F_{low}}$ sample. However, despite alloying occurring at the interface, a layered structure of the sample is still maintained. It is indicated by the still well distinguished RBS Co peak (inset of figure 9 and SM S5), what is visible on concentration profile obtained from the spectrum best-fit parameters (inset of figure 6 $\mathbf{F_{low}}$) for the RBS experimental data. XRD calculation (table 1) shows surface alloy-layer has an average composition of $Pt_{0.9}Co_{0.1}$ (L_{SA}). The *ab initio* calculation of magnetocrystalline anisotropy energy for intermixed Pt/Co interface (without surface or interface relaxation) suggest that interface anisotropy (K_S) should be smaller than of perfect interface [56]. Notwithstanding this, beyond a limited alloying, the lattice in-plane tensile strain induced by irradiation with low fluence can influence the PMA by the magnetoelastic anisotropy [29]. Moreover, a small addition of Pt into hcp Co can affect the lattice constants, favouring slightly the *a*-axis expansion, what affect the magneto-crystalline anisotropy [57]. Finally, we can imagine, strain in Pt/Co/Pt may be caused by the natural properties of heterostructure itself (crystalline interface misfit). **Ref** sample already exhibits in-plane compressed Pt structure what was deduced from RHEED as d-spacing evolution during growth (SM S2) and XRD derived negative ε_{xx} strain component (table 1). Thus it can be concluded that Co layer is under tensile strain influenced by Pt crystal lattice, especially for small thicknesses. Such strain can be modified by ion irradiation. The top part of the sample (L_{SA} in $\mathbf{F_{low}}$) undergoes tensile distortion in the in-plane direction. In $\mathbf{F_{low}}$ sample, the crystalline order of the component layers and chemical sharpness of the interfaces slightly decrease, what very probably influence interfacial strains network. This is most visible in c-RBS by the significantly elevated intensity of the Pt surface peak (see figure 9). This can be assigned to scattering from the defects or interstitials distributed in the near-surface region. Most probably substantial contribution may come from Pt and Co interstitial atoms relocated due to irradiation-triggered disordering. Additionally, diminishing of the Laue oscillations in XRD $\mathbf{F_{low}}$ data indicates the decrease of the thickness of coherent atomic planes, induced by inhomogeneous strains. Such strain modification, that is correlated to observed PMA changes, can be attributed to defects (vacancies) creation upon ion irradiation by dense electronic excitations [22] or independent binary collisions of atoms. Defects distribution predicted by TRIDYN calculations, and indirectly detected by elevated surface RBS peak and XRD Laue oscillations evolution well

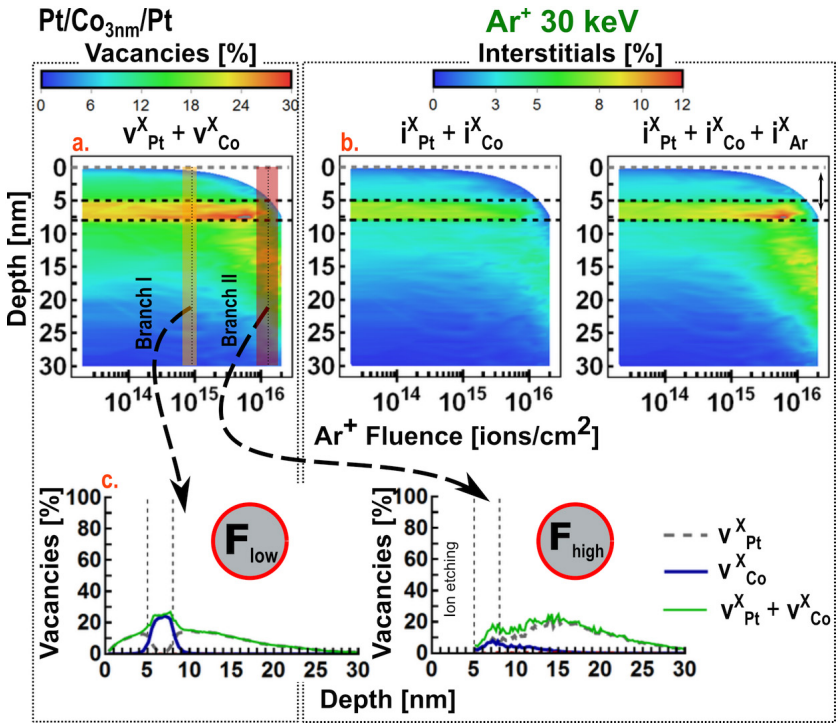

Figure 10. Vacancy generation (a) v_{el}^{X} (**F**, depth) diagrams and interstitial atoms generation (b) i_{el}^{X} (**F**, depth) diagrams.

correlates well with the PAS measurements. An estimated density creation of defects refined from TRIDYN (figure 10) shows the distribution of vacancies (v) and interstitials (i) in investigated Pt/Co/Pt structures. Depth, at which vacancies and interstitials are created, depends on ion energy (see SM S3 for 1.2 and 5 keV irradiation). TRIDYN simulations and indirectly visible as the c-RBS surface peak for $\mathbf{F_{low}}$ show that range up to $\mathbf{F} < 10^{15}$ ions cm^{-2} vacancies and interstitials are generated mostly in the Co layer. This explains relatively small differences between PAS spectra (figure 7(b)) for **Ref** and $\mathbf{F_{low}}$ samples observed in the positron energy range up to 3 keV. The S-parameter rise slightly at about 1.5 keV, with respect to **Ref** sample, which indicates not only larger defect concentration (also see low momentum part, $p_L < 5 \cdot 10^{-3}$ m_0c, in figure 8(a)) but likely a new phase, e.g. $Pt_{x-1}Co_x$ phase, which is even more pronounced in $\mathbf{F_{high}}$ sample. Moreover, according to TRIDYN, mean penetration depth of Ar^+ ions is ca. 13 nm, so most of Ar^+ energy is released in capping Pt, Co, and the most top part of the Pt seed layer. Thus, for $\mathbf{F_{low}}$ sample disappearing of the $S(E)$ maximum at $E = 3.4$ keV (figure 7(b)), visible in **Ref** sample, suggests indeed its origin from a Co layer, what can be ascribed to dislocation network at Pt/Co interface [47] extending from the seed Pt interface to the magnetic layer.

3.2. $\mathbf{F_{high}}$—*'Branch II'*

$\mathbf{F_{high}}$ fluence causes substantial mixing that forms quasi-uniform alloy as confirmed indirectly by the RBS Pt symmetric signal, indicating uniform layer with imperceptible signal lowering, due to the Co layer. XRD peak deconvolution allows distinguishing L_{H1}, intermixed top layer (see table 1), with an estimated 13% Co content in it. Moreover, L_{H1} layer exhibit in-plane tensile strain while underneath the L_{H2} layer is compressed. Three factors contribute to the appearance of PMA in $\mathbf{F_{high}}$: increase of in-plain strain component ($\varepsilon_{xx} > 0$), a decrease of demagnetization term $-2\pi M_S^2$ due to Co–Pt intermixing and an appearance of disc-like Co inclusions [32] in fully modified samples. Moreover, the c-RBS diminishing signal (figure 9) suggests that the sample undergoes crystalline structure recovery process, as a reappearance of XRD Laue oscillations (figure 5) in $\mathbf{F_{high}}$ is present. Reasons for this can be sought in the fact that at the higher range of **F**, a substantial amount of defect is generated (figures 7(b) and 8(a) inset, also SM S6) what correlates with larger $S(E)$ in the PAS $\mathbf{F_{high}}$ spectra reaching higher energies ($E > 3$ keV). The crystal lattice becomes defect saturated and also Co layer integration has been extirpated due to the intermixing. As the result Co layer no longer acts as a stabilizing layer, thus **F** caused changes to force the solid state epitaxy recovery process. Also, reduced RBS Pt peak width, topography measurements and TRIDYN predictions (SM S3) imply a significant etching of the sample surface (ca. 5 nm). Thus, precise calculation of alloy composition is not trivial, what manifests itself in discrepancy among TRIDYN, XRD and RBS alloy composition results, for $\mathbf{F_{high}}$ sample. It seems that TRIDYN inaccurately simulate surface Co dilution extent (max ~0.5 of Co—TRIDYN, 0,13 of Co in L_{H1} content—XRD, max ~ 0.2 of Co—RBS, see figures 4–6, $\mathbf{F_{high}}$) due to discarding the long-time processes, such as diffusion or chemical forces and the real surface irregularities. Nevertheless, the impact of the Co content in the alloy on the PMA cannot be unambiguously indicated but modified surface roughness can. Finally, PAS-DBS result for $\mathbf{F_{high}}$ sample shows, even with intermixed layers, sample retained the most

surface region with larger *S*, which may indicate still existing Pt capping what reduces the possibility of Co oxidation and persisting influence on PMA—also deduced from SIMNRA/SimTarget RBS reckoning (see inset figure 6(c) and SM S5).

3.3. The process of modifying the sample structure with ions and its effect on PMA

The efficiency and depth localisation of ion modifications strongly depend on the energy of ions, which can be seen both from on the magneto-optic effect (figure 3) and TRIDYN simulations (see SM S3). Starting from the lowest $\mathbf{F} < 10^{14}$ Ar^+ cm^{-2}, a 30 keV irradiation generates defects (figure 10), which modify strain distribution. This results in shifting the SRT to lower Co primary thickness (figures 3(b)–(f)). Interface intermixing is negligible at this **F**. For 1.2 and 5 keV Ar^+, the shifting of the SRT undergoes gradually (**F**-dependence) because the modification of the lower interface of Co/Pt is limited and the region of severe ion mixing lays above the upper interface Pt/Co. Moreover, depending on the initial film strain (sample growth conditions) and the mass of the projectile ions, strain resulted from the irradiation can either be tensile or compressive. With **F** applied, possible transitions towards tensile or compressive strain can occur. Such effect derives from anisotropic interstitial diffusion in a uniform biaxial stress field [58]. Since the penetration depth of Ar^+ ions strongly depends on its initial energy, the occurrence of the 'branch I' is shifted to higher **F** for lower ions energies (figures 3(b)–(f)). It is obvious that for extremely low ion energies, the 'branch I' cannot occur because penetration depth is too small and irradiation is reduced to the etching of the upper layer. Also, the tensile strain induction is less pronounced at higher **F** due to the already intermixed layers. It can be assumed that the 'branch I' appearance require properly selected (depth of Co layer) ion energy for high in-plane tensile strain generation. One can see, the Co layer lateral inhomogeneities (figure 2, Co STM). However, the influence on the PMA of such grainy continuous texture at the interface should only lead to some blurring of magnetic properties. What we discuss in the supplementary material in the (see SM S2). Subsequently, for $\mathbf{F} > \mathbf{F_{low}}$ (30 keV), the strain becomes isotropic [29], which coincides with the disappearance of enhanced PMA. Finally, at high **F** surface etching and topography modification coincides with occurrence 'branch II' of the enhanced PMA, where fully intermixed topmost layers strain become tensile in-plane with respect to relaxed lattice parameter and high volume concentration of vacancies is present. A thorough PAS analysis of these defects indicates that generally, ion irradiation increases defect concentration as **F** increases. The increase of *S* yields to the increase of defect concentration of that particular defect (figure 7(b)). Moreover, PAS *S*–*W* plot (figure 7(c)) shows a very good linear alignment of the experimental points, i.e. that suggests that regardless **F** the induced defects are of the same type and only defect concentration varies and relative ratio between Co and Pt elements around defect sites. It is clear that investigated trilayers have a strong relation to the electronic structure of Pt, thus Pt vacancies are dominant in our systems and defect sites surrounding consist to a large extent of Pt atoms as well. No clear correlation with the low-defect Co reference sample is found nor with the Co MBE-grown reference. That suggests no pure Co vacancy states within the Co layer but rather interstitial atoms and defected interfaces where defect surrounding consists of both elements (Pt and Co) and their relative ratio that varies depending on **F**. That, on the other hand, implies interface intermixing already for $\mathbf{F_{low}}$, which strongly extends for $\mathbf{F_{high}}$. PAS cDBS (figure 8(a)) shows that the detected electron momentum distribution for single element materials, i.e., Co and Pt nor their vacancy states cannot directly explain our experimental data for the as-grown and irradiated samples. From first-principles calculations of the vacancy formation energy (E_f) in Pt and Co, we know that energy is higher for Co(fcc) 2.1 eV than in Pt 1.2 eV [59–61]. In alloys the energy is reduced by Pt influence to ca. 1.38 eV for $L1_0$-ordered CoPt [62, 63]. The other phases should take E_f values between the extremes of Co and Pt values [64]. However, the PAS cDBS ratio plots and ATSUP simulations together show that a defect configuration even in the as-grown sample likely is more complicated than simple monovacancies or edge dislocation at the interface. Rather small vacancy complexes situated at both Co and Pt atomic positions could exist in Pt/Co/Pt trilayers, especially after ion irradiation. It is indirectly confirmed based on PALS measurements on thicker Co and Pt reference samples (see SM S6), where a clear signature of vacancy complexes has been found for the former, whereas the Pt-reference sample exhibit mostly mono- or bi- vacancy states. We could go one step further with our interpretation and imagine a situation where such vacancy complexes of large enough concentration would induce discontinuity within the Co layer or close to the interfaces similar to the Co-nanodiscs formation proposed recently [32]. As presented in figure 7(c), data represents calculated S and W values of measurements conducted with a relatively low statistic (about $1.5–2 \cdot 10^6$ cts/energy) and points are very close to each other, a clear conclusion on the defect types, existing in our systems, cannot be unambiguously drawn. Instead, the cDBS data shown in figure 8, (statistic of $7–10 \cdot 10^7$ cts/energy) brings more details about the atomic environment of defects. ATSUP simulations of the cDBS dependences for vacancy complexes figure 8(b). Calculated dependences are very similar to the monovacancy curves in the high momentum range. In our opinion, the electronic structure of Pt/Co/Pt trilayers consists of electron orbitals contributions from both Co (minimum at $p_L \sim 8 \cdot 10^{-3}$ m_0c) and Pt for $p_L > 15 \cdot 10^{-3}$ m_0c, which is only possible at the interfaces or for intermixtures. As RBS and XRD clearly prove that the as-grown layer structure is conserved, we can safely assume that the positron annihilation takes place to a larger extent at the interfaces, thus it should be sensitive to the local ordering and possibly could be related to the magnetic ordering as well. To evidence this the CoPt $L1_0$ model system has been simulated where Co to Pt ratio is 50%. Ordered CoPt $L1_0$ represents a class of materials with high PMA [63, 65]. As a result, a broader minimum at $p_L \sim 10 \cdot 10^{-3}$ m_0c has been obtained (figure 8(b)), which fits much better to the experimental data, however, the high momentum part consists mostly of Co orbitals. Simulated Pt(A1-fcc) and Co(A3-hcp)

models with vacancy states v_{Co} and v_{Pt} do not improve the high momentum part but on contrary, the atomic surrounding of a defect is more shifted to Co. The most logical conclusion is that the electronic structure at the annihilation site is dominated by Pt, which is only possible in Pt-rich alloys like Pt_xCo_{1-x}, where $x > 0.7$. In order to prove that, a model Pt_3Co (A1-fcc) and PtCo ($L1_0$-fct) structures have been simulated. For the latter, a Co sublattice was substituted by Pt antisite atoms. Different vacancy configurations have been calculated and compared with experimental data. The best agreement with experimental results has been obtained for a PtCo $L1_0$ structure containing only one Co atom and a small vacancy cluster combining a Co vacancy with two neighbouring Pt vacancies in the Co-sublattice (red marked data in figure 8(b), see inset). In that case, the high-momentum contribution shows a broader minimum at $p_L \sim 14 \cdot 10^{-3}\ m_0c$, which fits the experimental data. As the result, the positron annihilation cDBS data for Pt/Co/Pt trilayers can be explained by the presence of small vacancy clusters in a Pt-rich environment of a CoPt $L1_0$ structure. However, such vacancy complexes cannot be attributed to the occurrence of the enriched PMA because of figure 8(a) clearly shows that only level of these complexes increases, as **F** increases, showing no change in character in $\mathbf{F_{low}}$ or $\mathbf{F_{high}}$ sample. Nevertheless, it shows indirectly that $L1_0$ like complex is generated in ion irradiated Pt/Co/Pt trilayer.

4. Conclusions

The correlation of alloy formation, strain generation and defects creation related properties linked to enhanced PMA have been studied in Pt/Co/Pt samples irradiated by 30 keV Ar^+. Two 'branches' of increased PMA are found on 2D ($\mathbf{d_{Co}}$, **F**) diagrams for 30 keV Ar^+ irradiation. The enhanced magneto-optical response was found. Good agreement with previously reported [3] results of 30 keV Ga^+ irradiated of Pt/Co/Pt and previous interpretations [28, 29, 32] have been shown. While decreasing ions energy (1.2 keV and 5 keV) **F** difference between 'branches' decreases. For 1.2 keV Ar^+, large **F** range of low magnetic properties modifications and single 'branch' PMA was observed. Moreover, the paper discusses defect influence to the PMA, which to our knowledge has not been studied so far. By varying the positron energy of monoenergetic positron beam, we obtain analytically additional information on the chemical surrounding of open volume defects that were created during the irradiation process. PAS cDBS, assisted with ATSUP simulations, shows that structure with properties of tetragonal CoPt, with vacancy complex Co–Pt–Pt and two Pt antisites, is generated by the irradiation. Therefore, we claim that ion-induced defects played an important role in tuning the structural, atomic diffusion, and finally magnetic properties of Pt/Co/Pt heterostructure, particularly in tailoring the PMA. Choosing ion energy and **F** one can at low ion energy remove nonmagnetic overlayer (important for many *in situ* studies with magnetic surface sensitive techniques) at higher ion energy drive magnetic and magneto-optical properties opening novel routes for patterning of magnetic nanostructures.

Acknowledgements

This work was supported by the Foundation for Polish Science (FNP) and co-financed by the EU European Regional Development Fund, (TEAM SYMPHONY OPIE 07-13, and REINTEGRATION 2017 OPIE 14-20). The MePS facility has partly been funded by the Federal Ministry of Education and Research (BMBF) with the grant PosiAnalyse (05K2013). The support of the ELBE team at HZDR is greatly acknowledged. The authors would also like to thank Mr Dyczewski Jan, IoP PAS in Warsaw for supplementary RBS measurements.

ORCID iDs

M M Jakubowski https://orcid.org/0000-0002-7963-3454

References

[1] Fassbender J, Ravelosona D and Samson Y 2004 Tailoring magnetism by light-ion irradiation *J. Phys. D: Appl. Phys.* **37** R179–96
[2] Jaworowicz J *et al* 2009 Spin reorientation transitions in Pt/Co/Pt films under low dose Ga^+ ion irradiation *Appl. Phys. Lett.* **95** 022502
[3] Maziewski A *et al* 2012 Tailoring of magnetism in Pt/Co/Pt ultrathin films by ion irradiation *Phys. Rev.* B **85** 054427
[4] Breitkreutz S, Eichwald I, Kiermaier J, Hiblot G, Csaba G, Porod W, Schmitt-Landsiedel D and Becherer M 2014 Controlled domain wall pinning in nanowires with perpendicular magnetic anisotropy by localized fringing fields *J. Appl. Phys.* **115** 1–4
[5] Franken J H, Swagten H J M and Koopmans B 2012 Shift registers based on magnetic domain wall ratchets with perpendicular anisotropy *Nat. Nanotechnol.* **7** 499–503
[6] Fassbender J and McCord J 2008 Magnetic patterning by means of ion irradiation and implantation *J. Magn. Magn. Mater.* **320** 579–96
[7] Bruchhaus L, Mazarov P, Bischoff L, Gierak J, Wieck A D and Hövel H 2017 Comparison of technologies for nano device prototyping with a special focus on ion beams: a review *Appl. Phys. Rev.* **4** 011302
[8] Corredor E C, Kuhrau S, Kloodt-Twesten F, Frömter R and Oepen H P 2017 SEMPA investigation of the Dzyaloshinskii–Moriya interaction in the single, ideally grown Co/Pt(1 1 1) interface *Phys. Rev.* B **96** 060410
[9] Wells A W J, Shepley P M, Marrows C H and Moore T A 2017 Effect of interfacial intermixing on the Dzyaloshinskii–Moriya interaction in Pt/Co/Pt *Phys. Rev.* B **95** 054428
[10] Miao B, Millev Y, Sun L, You B, Zhang W and Ding H 2013 Thickness-driven spin reorientation transition in ultrathin films *Sci. China Phys. Mech. Astron.* **56** 70–84
[11] Chappert C 1998 Planar patterned magnetic media obtained by ion irradiation *Science* **280** 1919–22
[12] Devolder T 2000 Light ion irradiation of Co/Pt systems: structural origin of the decrease in magnetic anisotropy *Phys. Rev.* B **62** 5794–802
[13] Rettner C T, Anders S, Baglin J E E, Thomson T, Terris B D and He M 2002 Characterization of the magnetic modification of Co/Pt multilayer films by He^+, Ar^+, and Ga^+ ion irradiation *Appl. Phys. Lett.* **80** 279
[14] Devolder T, Ferré J, Chappert C, Bernas H, Jamet J-P and Mathet V 2001 Magnetic properties of He^+ -irradiated Pt/Co/Pt ultrathin films *Phys. Rev.* B **64** 064415

[15] Mazalski P, Kurant Z, Maziewski A, Liedke M O O, Fassbender J, Baczewski L T T and Wawro A 2013 Ion irradiation induced enhancement of out-of-plane magnetic anisotropy in ultrathin Co films *J. Appl. Phys.* **113** 17C109
[16] Bonder M J, Telling N D, Grundy P J, Faunce C A, Shen T and Vishnyakov V M 2003 Ion irradiation of Co/Pt multilayer films *J. Appl. Phys.* **93** 7226–8
[17] Chang G S, Moewes A, Kim S H, Lee J, Jeong K, Whang C N, Kim D H and Shin S-C 2006 Uniaxial in-plane magnetic anisotropy of a CoPt thin film induced by ion irradiation *Appl. Phys. Lett.* **88** 092504
[18] Vieu C *et al* 2002 Modifications of magnetic properties of Pt/Co/Pt thin layers by focused gallium ion beam irradiation *J. Appl. Phys.* **91** 3103–10
[19] Blon T, Baules P, Ben Assayag G, Kolinský V, Ousset J-C and Snoeck E 2007 Structural and magnetic properties of N^+-irradiated Co/Pt multilayers with perpendicular bimodal behaviour *J. Magn. Magn. Mater.* **315** 5–11
[20] Zhang K, Gupta R, Lieb K P, Luo Y, Müller G A, Schaaf P and Uhrmacher M 2003 Xenon-ion-induced phase transition in thin Co films *Europhys. Lett.* **64** 668–74
[21] Suharyadi E, Kato T and Iwata S 2014 Controlling the magnetic properties of Cr-implanted Co/Pt multilayer films using ion irradiation for planar patterned media *IEEE Trans. Magn.* **50** 1–4
[22] Sehdev N, Medwal R, Malik R, Chandra Agarwal D, Asokan K, Kanjilal D and Annapoorni S 2014 Defects mediated diffusion in Pt/Co/Pt multilayers induced by dense electronic excitations *Curr. Appl. Phys.* **14** 455–61
[23] Hyndman R, Warin P, Gierak J, Ferré J, Chapman J N, Jamet J P, Mathet V and Chappert C 2001 Modification of Co/Pt multilayers by gallium irradiation—part 1: the effect on structural and magnetic properties *J. Appl. Phys.* **90** 3843
[24] Warin P, Hyndman R, Glerak J, Chapman J N, Ferré J, Jamet J P, Mathet V and Chappert C 2001 Modification of Co/Pt multilayers by gallium irradiation—part 2: the effect of patterning using a highly focused ion beam *J. Appl. Phys.* **90** 3850–5
[25] Martín J I, Nogués J, Liu K, Vicent J L and Schuller I K 2003 Ordered magnetic nanostructures: fabrication and properties *J. Magn. Magn. Mater.* **256** 449–501
[26] Kusinski G J, Krishnan K M, Denbeaux G and Thomas G 2003 Magnetic reversal of ion beam patterned Co/Pt multilayers *Scr. Mater.* **48** 949–54
[27] Amemiya K, Sakamaki M, Mazalski P, Sveklo I, Kurant Z, Maziewski A, Liedke M O, Fassbender J, Wawro A and Baczewski L T 2013 Ga^+ ion irradiation-induced changes in magnetic anisotropy of a Pt/Co/Pt thin film studied by x-ray magnetic circular dichroism *EPJ Web Conf.* **40** 08002
[28] Avchaciov K A, Ren W, Djurabekova F, Nordlund K, Sveklo I and Maziewski A 2015 Modification of Pt/Co/Pt film properties by ion irradiation *Phys. Rev.* B **92** 104109
[29] Sakamaki M, Amemiya K, Liedke M O, Fassbender J, Mazalski P, Sveklo I and Maziewski A 2012 Perpendicular magnetic anisotropy in a Pt/Co/Pt ultrathin film arising from a lattice distortion induced by ion irradiation *Phys. Rev.* B **86** 024418
[30] Jakubisova-Liskova E, Visnovsky S, Wawro A, Baczewski L T, Mazalski P, Maziewski A, Liedke M O, McCord J and Fassbender J 2014 Effect of Ga^+ irradiation in molecular-beam epitaxy grown Pt/Co/Pt thin films studied by magneto-optic spectroscopy *J. Appl. Phys.* **115** 17C106
[31] Lišková E, Veis M, Višňovský Š, Ferré J, Mougin A, Mazalski P, Maziewski A, Liedke M O and Fassbender J 2012 Effect of Ga^+ irradiation on the magneto-optic spectra of Pt/Co/Pt sandwiches *Thin Solid Films* **520** 7169–72
[32] Sakamaki M, Amemiya K, Sveklo I, Mazalski P, Liedke M O, Fassbender J, Kurant Z, Wawro A and Maziewski A 2016 Formation of Co nanodisc with enhanced perpendicular magnetic anisotropy driven by Ga^+ ion irradiation on Pt/Co/Pt films *Phys. Rev.* B **94** 174422
[33] Möller W, Eckstein W, Biersack J P, M?ller W, Eckstein W and Biersack J P 1988 Tridyn-binary collision simulation of atomic collisions and dynamic composition changes in solids *Comput. Phys. Commun.* **51** 355–68
[34] Hugenschmidt C 2016 Positrons in surface physics *Surf. Sci. Rep.* **71** 547–94
[35] Krause-Rehberg R and Leipner H S 1999 *Positron Annihilation in Semiconductors* vol 127 (Berlin: Springer)
[36] Hautojärvi P, Dupasquier A, Manninen M J, Mijnarends P E, Nieminen R M, Vehanen A and West R N 1979 *Positrons in Solids* vol 12, ed P Hautojärvi (Berlin: Springer)
[37] Li M *et al* 2017 The effect of HfO_2 on the magnetic anisotropy, electrical structure and microstructure of CoFeB/MgO films *J. Alloys Compd.* **725** 425–32
[38] Colaux J L, Jeynes C, Heasman K C and Gwilliam R M 2015 Certified ion implantation fluence by high accuracy RBS *Analyst* **140** 3251–61
[39] Colaux J L and Jeynes C 2014 High accuracy traceable Rutherford backscattering spectrometry of ion implanted samples *Anal. Methods* **6** 120–9
[40] Siva V, Sahu S S, Datta D P, Pradhan P C, Nayak M, Solanki V, Topwal D, Senapati K and Sahoo P K 2016 Ion irradiation induced phase transition of Co in Co/Au multilayers *J. Alloys Compd.* **680** 722–8
[41] Mayer M 1999 SIMNRA, a simulation program for the analysis of NRA, RBS and ERDA *AIP Conf. Proc.* **475** 541–4
[42] Mayer M 2014 Improved physics in SIMNRA 7 *Nucl. Instrum. Methods Phys. Res.* B **332** 176–80
[43] Colaux J L, Terwagne G, Demelenne L and Derycke I 2009 SimTarget applet http://webapps.fundp.ac.be/physique/simtarget/
[44] Anwand W, Kissener H-R and Brauer G 1995 A magnetically guided slow positron beam for defect studies *Acta Phys. Pol.* A **88** 7–11
[45] Anwand W, Brauer G, Butterling M, Kissener H R and Wagner A 2012 Design and construction of a slow positron beam for solid and surface investigations *Defect Diffus. Forum* **331** 25–40
[46] Wagner A *et al* 2017 Positron annihilation lifetime spectroscopy at a superconducting electron accelerator *J. Phys.: Conf. Ser.* **791** 012004
[47] Varga P, Lundgren E, Redinger J and Schmid M 2001 Ultrathin films of Co on Pt(1 1 1): an STM view *Phys. Status Solidi* **187** 97–112
[48] Ichimiya A and Cohen P I 2004 *Reflection High-Energy Electron Diffraction* (Cambridge: Cambridge University Press)
[49] Dynowska E *et al* 2015 Structural investigation of ultrathin Pt/Co/Pt trilayer films under EUV irradiation *Nucl. Instrum. Methods Phys. Res.* B **364** 33–9
[50] Jacyna I *et al* 2018 Study of ultrathin Pt/Co/Pt trilayers modified by nanosecond XUV pulses from laser-driven plasma source *J. Alloys Compd.* **763** 899–908
[51] van Veen A, Schut H, Clement M, de Nijs J M M, Kruseman A and IJpma M R 1995 VEPFIT applied to depth profiling problems *Appl. Surf. Sci.* **85** 216–24
[52] Liedke M O *et al* 2015 Open volume defects and magnetic phase transition in $Fe_{60}Al_{40}$ transition metal aluminide *J. Appl. Phys.* **117** 163908
[53] Kosub T *et al* 2017 Purely antiferromagnetic magnetoelectric random access memory *Nat. Commun.* **8** 13985
[54] Puska M J and Nieminen R M 1983 Defect spectroscopy with positrons: a general calculational method *J. Phys. F: Met. Phys.* **13** 333

[55] Seitsonen A P, Puska M J and Nieminen R M 1995 Real-space electronic-structure calculations: combination of the finite-difference and conjugate-gradient methods *Phys. Rev.* B **51** 14057–61
[56] MacLaren J M and Victora R H 1994 Theoretical predictions of interface anisotropy in the presence of interdiffusion *J. Appl. Phys.* **76** 6069–74
[57] Kikuchi N, Kitakami O, Okamoto S, Shimada Y, Sakuma A, Otani Y and Fukamichi K 1999 Influence of 5d transition elements on the magnetocrystalline anisotropy of hcp-Co *J. Phys.: Condens. Matter* **11** L485–90
[58] Chan W-L, Zhao K, Vo N, Ashkenazy Y, Cahill D G and Averback R S 2008 Stress evolution in platinum thin films during low-energy ion irradiation *Phys. Rev.* B **77** 205405
[59] Mattsson T R and Mattsson A E 2002 Calculating the vacancy formation energy in metals: Pt, Pd, and Mo *Phys. Rev.* B **66** 214110
[60] Korzhavyi P A, Abrikosov I A, Johansson B, Ruban A V and Skriver H L 1999 First-principles calculations of the vacancy formation energy in transition and noble metals *Phys. Rev.* B **59** 11693–703
[61] Ullmaier H 1991 *Atomic Defects in Metals* vol 25 (Berlin: Springer)
[62] Ersen O, Goyhenex C and Pierron-Bohnes V 2008 Diffusion piloted ordering in codeposited CoPt epitaxial layers: experiment and quenched molecular dynamics simulations *Phys. Rev.* B **78** 035429
[63] Andreazza P, Pierron-Bohnes V, Tournus F, Andreazza-Vignolle C and Dupuis V 2015 Structure and order in cobalt/platinum-type nanoalloys: from thin films to supported clusters *Surf. Sci. Rep.* **70** 188–258
[64] Kim S M 1984 Vacancy formation energies in disordered alloys *Phys. Rev.* B **30** 4829–32
[65] Barmak K, Kim J, Lewis L H, Coffey K R, Toney M F, Kellock A J and Thiele J-U 2005 On the relationship of magnetocrystalline anisotropy and stoichiometry in epitaxial L10 CoPt (0 0 1) and FePt (0 0 1) thin films *J. Appl. Phys.* **98** 033904